OPTICS

Extension of the bright high-harmonic photon energy range via nonadiabatic critical phase matching

Zongyuan Fu[1]†, Yudong Chen[1]†, Sainan Peng[1], Bingbing Zhu[1], Baochang Li[2], Rodrigo Martín-Hernández[3], Guangyu Fan[4,5], Yihua Wang[1,6], Carlos Hernández-García[3], Cheng Jin[2,7]*, Margaret Murnane[8], Henry Kapteyn[8], Zhensheng Tao[1]*

Copyright © 2022 The Authors, some rights reserved; exclusive licensee American Association for the Advancement of Science. No claim to original U.S. Government Works. Distributed under a Creative Commons Attribution NonCommercial License 4.0 (CC BY-NC).

The concept of critical ionization fraction has been essential for high-harmonic generation, because it dictates the maximum driving laser intensity while preserving the phase matching of harmonics. In this work, we reveal a second, nonadiabatic critical ionization fraction, which substantially extends the phase-matched harmonic energy, arising because of the strong reshaping of the intense laser field in a gas plasma. We validate this understanding through a systematic comparison between experiment and theory for a wide range of laser conditions. In particular, the properties of the high-harmonic spectrum versus the laser intensity undergoes three distinctive scenarios: (i) coincidence with the single-atom cutoff, (ii) strong spectral extension, and (iii) spectral energy saturation. We present an analytical model that predicts the spectral extension and reveals the increasing importance of the nonadiabatic effects for mid-infrared lasers. These findings are important for the development of high-brightness soft x-ray sources for applications in spectroscopy and imaging.

INTRODUCTION

High-harmonic generation (HHG) in atoms and molecules (*1*–*4*) has enabled many advances in attosecond science and technology (*5*–*7*) and, more recently, in quantum optics (*8*). HHG arises from the interaction of an intense laser field with an atomic or molecular gas target. The underlying process at the atomic and quantum level is based on strong-field ionization of an atom—a laser field modulates the spatial and temporal wave function of the outermost electron, leading to a rapidly changing dipole moment and emission of high harmonics of the driving laser field (*9*, *10*). Simple predictions of the maximum photon energy can be made using a semiclassical model (*11*, *12*). In this picture, the liberated electron is accelerated by a laser field and can be driven back to recollide with the parent ion when the laser field reverses, generating an extreme ultraviolet (XUV) or soft x-ray photon. The maximum photon energy achievable is determined by the maximum kinetic energy of the returning electron, which is given by the cutoff energy (*12*): $E_{cutoff} = I_p + 3.17U_p$. Here, I_p is the ionization potential and U_p is the ponderomotive energy, $U_p(\mathrm{eV}) = 0.0933 I_L(\mathrm{TW\ cm^{-2}})\lambda_L^2(\mu\mathrm{m}^2)$, where I_L and λ_L are the peak intensity and wavelength of the driving field, respectively.

Extending the bright photon energy range of HHG is important for many applications in science and technology: First, bright and broadband soft x-ray radiation spans many element-specific absorption edges, e.g., the "water-window" energy, and enables table-top element-resolved spectroscopy and microscopy (*13*–*15*). Second, broader HHG bandwidths can support the generation of shorter attosecond pulses (*16*, *17*) or powerful broadband imaging and spectroscopy methods (*18*). However, the HHG emission from a single atom exhibits a dipole pattern and is very weak. To generate a bright and directed high-harmonic beam, the driving laser and the generated harmonics must both travel at the same phase velocity in the gas, so that the HHG emission from many atoms combines constructively. Here, the concept of critical ionization fraction (η_c^{PMC}) is essential (*1*, *19*, *20*). Only when the laser-induced gas ionization is lower than a critical ionization level η_c^{PMC}, the phase-mismatch between the fundamental driving field and the harmonic field can be compensated, allowing for coherent buildup of HHG radiation along the propagation direction. Typical critical ionization levels η_c^{PMC} in a gas medium is <5%, which places a limit on the maximum driving laser intensity for which phase matching is possible, and thereby determines the phase-matching cutoff (PMC). Although more exotic schemes can support effective phase matching at very high levels of ionization (*21*), simultaneously achieving high photon energy and high brightness is still challenging.

Driving HHG with intense few-cycle pulses has attracted great interest, because it is one route for generating isolated attosecond pulses (*16*, *17*, *22*–*25*). When driven by few-cycle pulses, the maximum HHG photon energy was reported to be greatly extended (*26*–*28*). This is not only because pulse compression can boost the laser intensity but also because it facilitates phase matching for high-frequency harmonics by reducing gas ionization—for example, by reducing the pulse duration from 20 to 5 fs, the PMC can be extended by ~20%. However, to understand a HHG spectrum beyond the PMC, it also needs to consider the substantial reshaping of an intense few-cycle pulse in a dispersive plasma. In Fig. 1A, we plot a simple and intuitive schematic of HHG in such

[1]State Key Laboratory of Surface Physics, Key Laboratory of Micro and Nano Photonic Structures (MOE), and Department of Physics, Fudan University, Shanghai 200433, China. [2]Department of Applied Physics, Nanjing University of Science and Technology, Nanjing, Jiangsu 210094, China. [3]Grupo de Investigación en Aplicaciones del Láser y Fotónica, Departamento de Física Aplicada, Universidad de Salamanca, E- 37008 Salamanca, Spain. [4]Shanghai Key Lab of Modern Optical System, University of Shanghai for Science and Technology, Shanghai 200093, China. [5]The Hamburg Centre for Ultrafast Imaging CUI, Universität Hamburg, 149 Luruper Chaussee, 22761 Hamburg, Germany. [6]Shanghai Research Center for Quantum Sciences, Shanghai 201315, China. [7]MIIT Key Laboratory of Semiconductor Microstructure and Quantum Sensing, Nanjing University of Science and Technology, Nanjing, Jiangsu 210094, China. [8]Department of Physics and JILA, University of Colorado and NIST, Boulder, CO 80309, USA.
*Corresponding author. Email: cjin@njust.edu.cn (C.J.); zhenshengtao@fudan.edu.cn (Z.T.)
†These authors contributed equally to this work.

Downloaded from https://www.science.org at Universidad de Salamanca on June 29, 2023

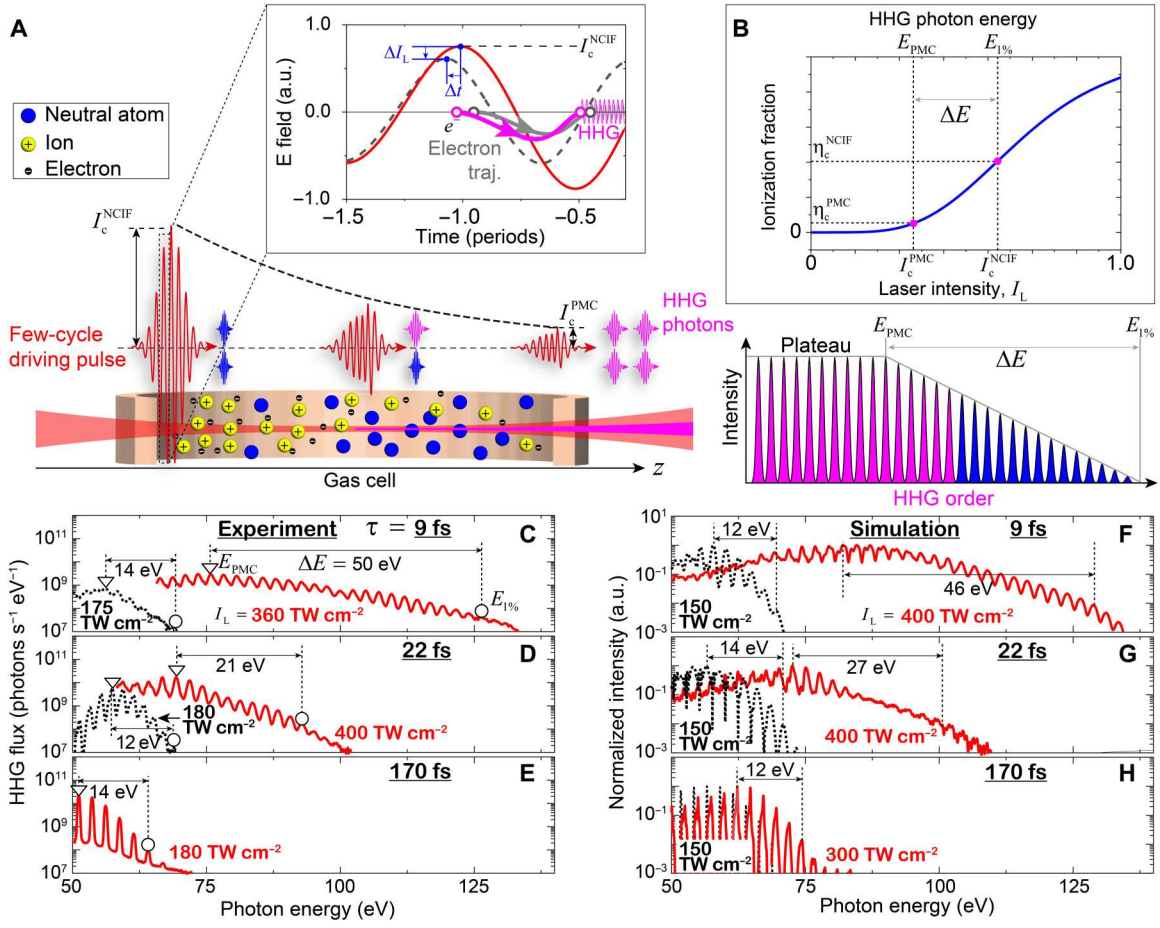

Fig. 1. Illustration of the general concept. (**A**) Illustration of the nonadiabatic HHG process driven by an intense few-cycle pulse in a gas cell, which exhibits the effects of plasma-induced intensity decay, temporal pulse reshaping, and variation of gas ionization along *z*. The HHG spectrum is the integrations of the emitters along *z* under a varying driving field. Inset: Illustration of the modulation of electron trajectories owing to the nonadiabatic field temporal reshaping. The solid line represents the incident driving laser field. The dashed line represents the field profile deformed by the nonadiabatic effects. The microscopic electron trajectories under two different driving fields are illustrated. (**B**) Illustration of the gas ionization fraction at the pulse temporal center, and the relationship among the critical intensities (I_c^{PMC} and I_c^{NCIF}), critical ionization fractions (η_c^{PMC} and η_c^{NCIF}), and the HHG photon energies (E_{PMC} and $E_{1\%}$). (**C** to **E**) HHG spectrum driven by pulse durations of τ = 9, 22, and 170 fs, respectively, under different laser intensities (I_L). (**F** to **H**) Results of numerical simulations under similar conditions as in (C) to (E). a.u., arbitrary units.

a regime, which involves several effects, such as an intensity drop due to plasma-induced defocusing, deformation of the laser field, a longitudinal gradient of gas ionization, etc. The emitted harmonic spectrum is the result of the coherent addition of the emission from numerous emitters along the propagation direction. Thus, an important question to address is, What is the maximum achievable HHG photon energy under these nonadiabatic conditions, which can support practically usable source brightness, i.e., to realize reasonable phase matching?

In recent years, there has been renewed interest in studying nonadiabatic effects in HHG, owing to advances in high-energy few-cycle mid-infrared lasers (*14*, *29*). Experimentally, it has been shown that the plasma- and nonlinear pulse reshaping is important for both several-cycle 4-μm lasers and few-cycle 1.8-μm lasers for the generation of high-flux >1000- and 600-eV soft x-ray harmonics, respectively (*29*, *30*). Experimentally, the subcycle deformation of the driving field occurs in many perturbative and nonperturbative nonlinear-optical processes and can be directly measured with the attosecond streaking technique (*31*). Theoretically, several important aspects of nonadiabatic effects have been revealed. It was shown that the plasma defocusing can clamp the laser intensity, limiting the harmonic energy (*32*). In addition, it has also been reported that the electronic trajectories from nonadiabatic drivers are modified (*33*), which supports phase matching of high-energy harmonics significantly higher than PMC (*34*, *35*). Generation of isolated attosecond pulses is also possible (*22*, *36*, *37*). It is worth noting that, thus far, there is no simple and analytical model that can guide the development of a phase-matched harmonic source under the nonadiabatic conditions, in contrast to the adiabatic HHG, where several successful models been developed [see, for example, (*1*, *19*, *38*, *39*)].

In this work, we introduce the previously unidentified concept of nonadiabatic critical ionization fraction (NCIF) that explains the reshaping and extension of a phase-matched harmonic spectrum under the nonadiabatic conditions. Our experimental and theoretical results demonstrate that the concept of NCIF is crucial to understand and achieve nonadiabatic phase-matched HHG effects, such as the extension of the spectral roll-offs beyond the PMC.

Downloaded from https://www.science.org at Universidad de Salamanca on June 29, 2023

Special attention has been paid to HHG driven by intense few-cycle pulses, which can produce the highest roll-off-energy extension. In particular, when driven by 9-fs, 1030-nm, and ~ 360 TW cm^{-2} peak intensity laser pulses in argon ($E_{cutoff} \approx 129$ eV), the harmonic spectrum can be extended to ~125 eV, which is ~50 eV higher than the corresponding PMC. Moreover, the brightness is between 10^9 and 10^7 photons s^{-1} eV^{-1}, which is sufficient for many applications in spectroscopy, and compares well with a peak brightness of $>10^{10}$ photons s^{-1} eV^{-1} at lower photon energies under perfect phase matching conditions. We identify three distinctive intensity regimes separated by two critical driving intensities, which determines the harmonic spectral shape: (i) coincidence with the single-atom cutoff, (ii) strong spectral extension, and (iii) spectral energy saturation. We have developed an analytical NCIF model that can precisely predict the spectral reshaping and extension under different driving-laser intensities, wavelengths, and pulse durations and in different gas species. Furthermore, our model also reveals that the spectral extension can be much greater when driven by long-wavelength, mid-infrared few-cycle lasers. Our results provide an alternative route guideline for extending the harmonic frequency to >1 keV, well into the soft x-rays, with high brightness placing nonadiabatic HHG as a practical soft x-ray source for applications in ultrafast spectroscopy and imaging (*29*, *40*, *41*).

RESULTS

Harmonic spectrum roll-offs under different driving conditions

The picture of macroscopic nonadiabatic HHG is depicted in Fig. 1A. When the driving laser peak intensity I_L is high, beyond the tunnel ionization regime, nonadiabatic effects appear in HHG. In the intensity regime we are interested, where the target atoms are not fully ionized, the driving field is reshaped when propagating through the gas cell as follows (*42*). First, the rear part of the pulse undergoes spatial defocusing due to gas ionization induced during the earlier cycles, which leads to a peak intensity drop and a shift of the envelope peak to the leading edge (see the inset of Fig. 1A). Second, the rapid subcycle variation of gas ionization causes a strong frequency blue shift of the pulse leading edge (see the inset of Fig. 1A) (*39*).

To investigate how such propagation of the fundamental field affects phase matching in HHG, we conducted systematic experiments under different laser conditions and in different gas species. In our experiments, laser pulses with full-width-at-half-maximum (FWHM) temporal durations of τ = 9, 22, and 170 fs, and peak intensities above 180 TW cm^{-2}, at a center wavelength of λ_L = 1030 nm are focused into a gas cell filled with argon and krypton. The gas-cell length is d = 1.5 mm. The high-harmonic spectrum is recorded by an XUV spectrometer after filtering out the fundamental driving laser with metal thin films. The details of the experimental setup are summarized in Materials and Methods and in section S1. In Fig. 1 (C to E), we plot the experimental harmonic spectra in argon driven by τ = 9, 22, and 170 fs pulses, respectively, and for different intensities. Here, we note that the reported laser intensities (I_L) in this work are those at the entrance of the gas cell, which can be reduced by plasma-induced defocusing inside the gas cell (see Fig. 1A). The gas pressures p are 50, 190, and 210 torr, respectively, for the three cases.

Under these high-intensity conditions, as the harmonic spectrum is obtained by summing up all the emitters along the propagation direction (z) under a varying field intensity (as illustrated in Fig. 1A), the classic microscopic cutoff energy (E_{cutoff}) is no longer discernible. To quantitatively analyze the harmonic spectral shape, we focus on two special harmonic energies (as labeled in Fig. 1, C and D): (i) the PMC energy (E_{PMC}), which corresponds to the energy from which the harmonic yield continuously decreases (*30*); and (ii) the 1%-intensity energy ($E_{1\%}$) where the spectral intensity decreases to 1% of the intensity at E_{PMC}. The energy difference $\Delta E = E_{1\%} - E_{PMC}$ represents the width of the spectral roll-off beyond the E_{PMC}. As shown in Fig. 1C (τ = 9 fs and I_L = 360 TW cm^{-2}, $E_{cutoff} \approx 129$ eV), ΔE can be as large as ~50 eV, which is comparable to the corresponding E_{PMC} (~75 eV), delivering a great amount of usable high-energy XUV photons beyond the PMC. The flux at ~125 eV can reach ~2×10^7 photons s^{-1} eV^{-1}. In contrast, the flux at the same energy is reduced by more than two orders of magnitude when driven by 22-fs, 400 TW cm^{-2} pulses, becoming not measurable with the 170-fs, 180 TW cm^{-2} pulses. For the τ = 22- and 170-fs cases, ΔE is reduced to ~21 and ~ 14 eV, respectively.

To investigate the physics beyond the experimental results, we have performed numerical simulations under similar conditions, as shown in Fig. 1 (F to H). The simulations were performed within the strong-field approximation (SFA) framework, taking into account the high-intensity regime (see Materials and Methods). The ionization rates have been calculated through an empirically modified Ammosov-Delone-Krainov (ADK) model (*43*) to take into account laser intensities above the tunnel ionization regime. Furthermore, the agreement between the SFA and the three-dimensional time-dependent Schrödinger equation (TDSE) in the single-atom simulation results further indicates that barrier suppression effects have limited influence in the intensity range of our experiments (see fig. S7). We find that, when the driving intensity I_L is low (e.g., I_L < 200 TW cm^{-2} for τ = 9 fs), ΔE is typically 10 to 14 eV, which is independent to the laser conditions (duration, intensity, wavelength, etc.) and the gas species (see section S3). Furthermore, we find that this value is consistent with the single-atom response (see figs. S6 and S7), indicating that it represents the quantum limit on the minimum energy extension (ΔE_{qt}). Thus, the deviation of ΔE from ΔE_{qt} can be attributed to the influence of macroscopic phase-matching and nonadiabatic effects.

Because the reshaping of the harmonic spectrum is most pronounced when the driving pulse duration is short, we now focus our attention on the results of τ = 9 fs. In Fig. 2, we show the influence of the gas plasma on the driving field, by plotting the simulation results of the driving field pulse at the entrance (black) and at the exit (red) of the gas cell for low (A, 200 TW cm^{-2}) and high (B, 700 TW cm^{-2}) values of I_L. From the comparison of Fig. 2 (A and B), we find that the driving field is strongly reshaped by the gas plasma in the high-intensity regime, resulting in a decrease in the field intensity, a strong frequency blue shift at the pulse leading edge, and a shift of the envelope peak to the leading edge by about one optical cycle. The time-frequency analysis on the numerical results of the corresponding HHG spectra are further shown in Fig. 2 (C and D). Correspondingly, the high-energy harmonic photons are dominantly generated at about one optical cycle before the pulse temporal center when the driving laser intensity is high (Fig. 2D). This result clearly demonstrates that the nonadiabatic effects play an essential role in the generation and phase

Downloaded from https://www.science.org at Universidad de Salamanca on June 29, 2023

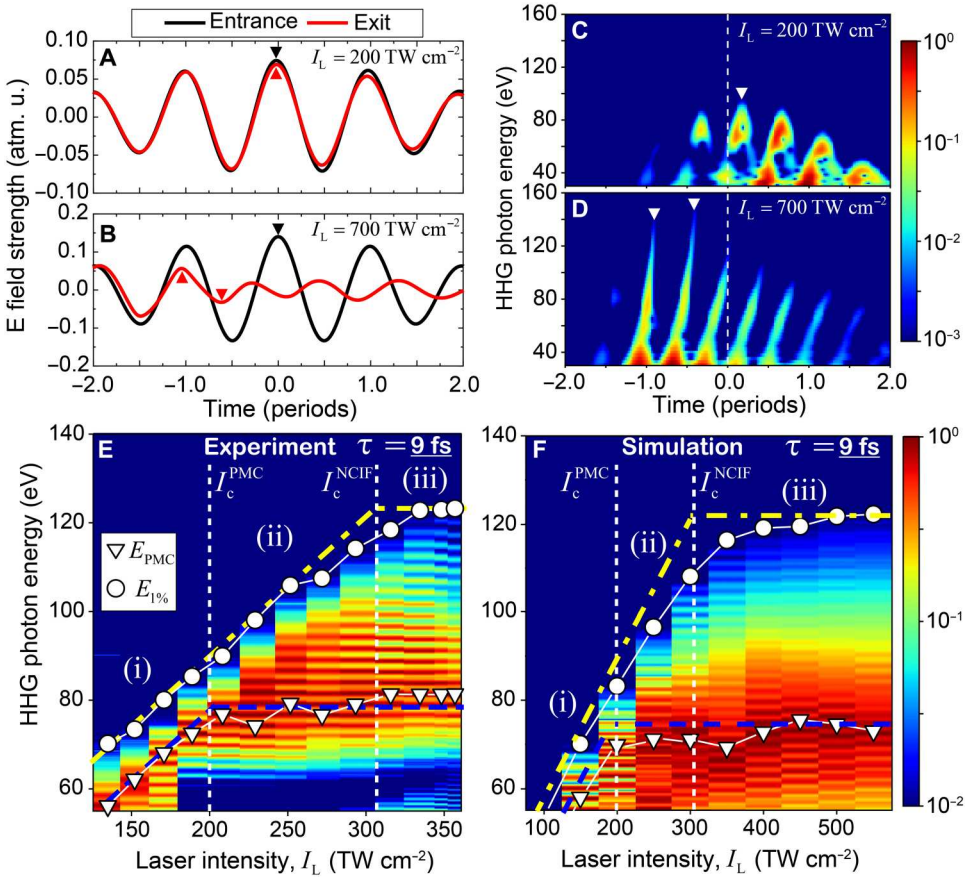

Fig. 2. Influence of nonadiabatic effects on harmonic spectrum. (**A**) Temporal field shapes obtained from the numerical simulations at the entrance and the exit of a gas cell (d = 1.5 mm) under laser intensity of I_L = 200 TW cm^{-2}. The gas cell is filled with argon with the pressure (p) of 100 torr. The time for the peak field is labeled by the solid triangles. (**B**) Same as (A) for I_L = 700 TW cm^{-2}. (**C** and **D**) Time-frequency analysis of the HHG generated under the laser conditions in (A) and (B). The emission time for the highest harmonic orders are labeled by the solid triangles. (**E**) Experimental HHG spectrum in argon driven by different laser intensity I_L with d = 1.5 mm and p = 50 torr. The pulse duration is τ = 9 fs. The blue dashed line represents E_{cutoff} when $I_L < I_c^{PMC}$ and a constant when above I_c^{PMC}. The yellow dashed-dotted line represents $\Delta E_{qt} + E_{cutoff}$ when $I_L < I_c^{NCIF}$ and a constant when above I_c^{NCIF}. Three regimes are distinguished by the two critical intensities (I_c^{PMC} and I_c^{NCIF}). (**F**) Same as (E) obtained from the numerical simulations under the same conditions.

matching of the high-energy harmonics beyond PMC. We note that the propagation effects have been considered in the numerical simulations of the HHG spectra. The spectral results are obtained by integrating across the transverse beam cross section.

To what extent the harmonic energy can be extended by the high laser intensities? To address this question, we measure the HHG spectrum driven by increasing I_L with τ = 9 fs in argon (Fig. 2E) and krypton (see section S3) with d = 1.5 mm and p = 50 torr. Here, we will first restrict our discussion to the case where d and p are optimized for the bright HHG emission around E_{PMC}. The situations with varying d and p will be discussed later. The energies of E_{PMC} and $E_{1\%}$ can then be labeled in the same way as illustrated in Fig. 1 (C to E). As shown in Fig. 2E, we can clearly distinguish three intensity regimes separated by two critical intensities (I_c^{PMC} and I_c^{NCIF}): (i) When $I_L < I_c^{PMC}$ and the gas ionization is low, the deformation of the driving field is negligible (Fig. 2A), and thereby, E_{PMC} is in excellent agreement with E_{cutoff} (the blue-dashed line). Furthermore, ΔE in this regime equals ΔE_{qt}, and, as a result, $E_{1\%}$ also increases linearly (the yellow dashed-dotted line), simply following $E_{1\%} = \Delta E_{qt} + E_{cutoff}(I_L)$. (ii) When $I_L > I_c^{PMC}$, the gas ionization is high enough to deform the driving field upon propagation. We identify I_c^{PMC} as the threshold intensity from which nonadiabatic effects play an important role. In this regime, we find that E_{PMC} saturates at the energy of E_{PMC}^{sat} ~75 eV, which corresponds to E_{cutoff} at $I_L = I_c^{PMC}$ (~78 eV in Fig. 2E). In contrast to E_{PMC}, $E_{1\%}$ continues to increase almost linearly in this regime, until I_L reaches the next critical intensity I_c^{NCIF} (~300 TW cm^{-2}). In this regime, the harmonic roll-off, given by ΔE, continues to increase with I_L, leading to the most pronounced spectral reshaping. However, (iii) when $I_L > I_c^{NCIF}$, our results show that $E_{1\%}$ eventually saturates at the energy of $E_{1\%}^{sat}$ (~125 eV for τ = 9 fs in argon), which corresponds to the sum of ΔE_{qt} and E_{cutoff} when $I_L = I_c^{NCIF}$. We note that the appearance of regime (iii) also indicates the saturation of the spectral reshaping and further increasing the harmonic energy becomes not possible. As shown in Fig. 2F, these observations can be quantitatively reproduced by the numerical simulations, including the values of I_c^{PMC} and I_c^{NCIF}. Moreover, the above three regimes can be universally observed under different pulse durations, gas atoms, and wavelengths (see section S3). However, the critical

Downloaded from https://www.science.org at Universidad de Salamanca on June 29, 2023

intensities and the corresponding saturation energies can be altered by these conditions. We note that the absence of low-order harmonics in Fig. 2 (E and F) when $I_L > 180$ TW cm^{-2} is caused by the use of a zirconium filter for blocking the driving laser. In the numerical simulations, the transmission spectrum of a zirconium filter (*44*) is implemented for the agreement. For lower driving intensities, an aluminum filter is used instead (see section S2).

The NCIF model

As illustrated in Fig. 1A, in the high-intensity regime we are analyzing, the high-energy HHG photons can only be generated at the early stage of the driving-laser propagation, before the laser intensity is reduced by plasma defocusing. In this region, the subcycle deformation of the driving field can play an essential role in phase matching (*31*, *34*, *35*). The wave vector mismatch between the fundamental driving field and the qth-order harmonic field can be expressed as a sum of four terms (*1*, *39*)

$$\Delta k_q = \Delta k_g + \Delta k_n + \Delta k_p + \Delta k_d \quad (1)$$

Here, Δk_g denotes the geometrical Gouy-phase term due to focusing. Δk_n and Δk_p account for the pressure-dependent contributions from the neutral-atom and free-electron dispersions, respectively, and are given by

$$\Delta k_n = \frac{2\pi q}{\lambda_L}\frac{p}{p_{atm}}[1-\eta(t)]\Delta\delta \quad (2)$$

$$\Delta k_p = -q\frac{p}{p_{atm}} r_e \eta(t) N_{atm} \lambda_L \left(1-\frac{1}{q^2}\right) \quad (3)$$

where p_{atm} is the atmospheric pressure, $\eta(t)$ is the ionization fraction, $\Delta\delta$ is the difference between the indices of refraction of the neutral gas per atmosphere at the fundamental and x-ray wavelengths, r_e is the classical electron radius, and N_{atm} is the number density per atmosphere. Last, Δk_d represents the wave vector mismatch induced by the dipole phase (*45*). Under the adiabatic conditions, this term is usually small for the phase matching of short-trajectory harmonics (*1*, *46*). Under the nonadiabatic conditions, however, due to the strong reshaping of the laser field under propagation, this term can become especially relevant for the phase matching of high-energy harmonics (*31*, *34*, *35*). Here, we derive that Δk_d is dominantly contributed by the phase mismatch due to the frequency blue shift of the driving field, which is the result of the

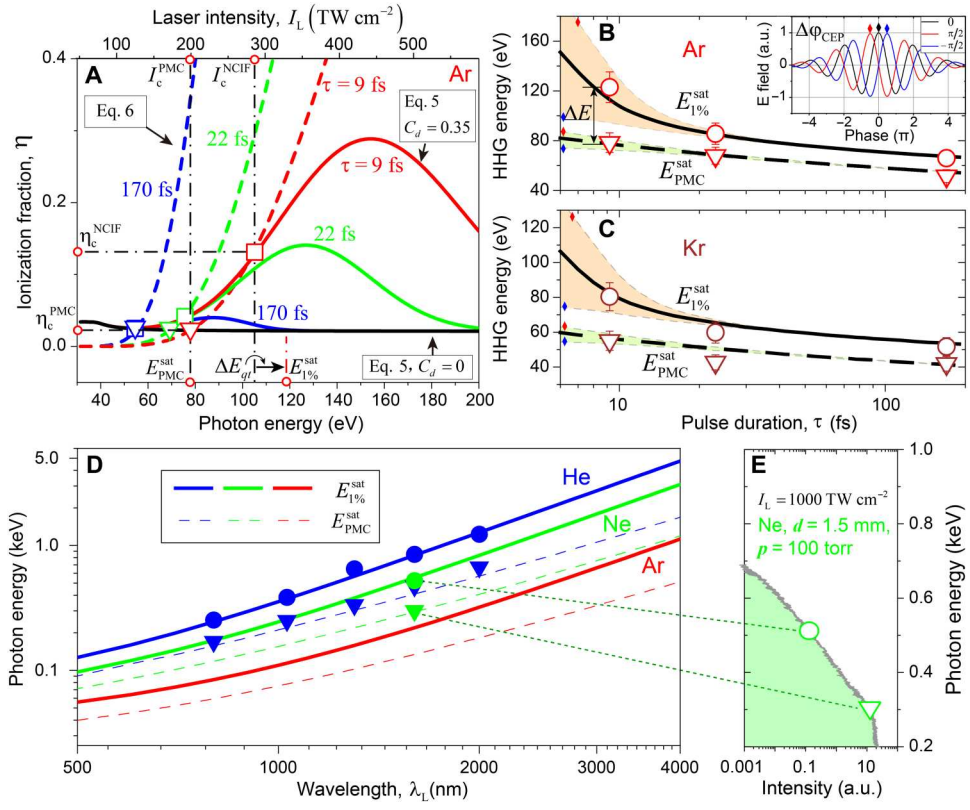

Fig. 3. The NCIF model results. (**A**) Results of the NCIF model for HHG in argon under different pulse durations (τ). The solid lines are the results of Eq. 5, with $C_d = 0.35$ (red, green, and blue) and $C_d = 0$ (black). The dashed lines are the results of Eq. 6. The intersections are labeled by open symbols. The open triangles label the results for PMC, and the open squares are for the 1%-intensity energy. (**B**) Comparison between the experimental results of E^{sat}_{PMC} (open triangles), $E^{sat}_{1\%}$ (open circles), and the NCIF model results (solid and dashed lines) in argon. The shaded area represents the variation of E^{sat}_{PMC} and $E^{sat}_{1\%}$ under different CEP phases ($\Delta\phi_{CEP}$). Inset: The illustration of the driving field waveforms under different $\Delta\phi_{CEP}$, with peak-field time labeled. (**C**) Same as (B) for the results in krypton. (**D**) NCIF model results under different wavelengths (λ_L) in argon, neon, and helium. The symbols represent the results obtained from the numerical simulations. (**E**) Typical numerical spectrum of HHG in neon. The E_{PMC} and $E^{1\%}$ are labeled. The gas pressure is 100 torr, the cell length is 1.5 mm, and the driving intensity is 1000 TW cm^{-2}.

Downloaded from https://www.science.org at Universidad de Salamanca on June 29, 2023

subcycle variation of gas ionization ($\frac{\partial \eta}{\partial t}$) (*47*) by

$$\Delta k_d \approx \alpha_j \frac{3U_p \lambda_L^3}{2\pi hc^2} \frac{p}{p_{atm}} r_e N_{atm} \frac{\partial \eta(I_L, t)}{\partial t} \quad (4)$$

where $\alpha_j = 3.2$ represents the phase coefficient at the cutoff energy (*39*), h is Planck constant, and c is the speed of light. The details of the derivation of Eq. 4 are provided in section S4.

Because Δk_g is negative and independent to the pressure, phase matching of HHG is only possible when $\Delta k_n + \Delta k_p + \Delta k_d > 0$. Hence, a critical ionization fraction including the nonadiabatic effects can be derived

$$\eta_c(I_L) \approx \frac{\frac{2\pi}{\lambda_L}\Delta\delta + C_d \frac{\alpha_j}{2\pi c} \frac{3U_p}{I_p + 3.17U_p} \lambda_L^2 r_e N_{atm} \frac{\partial \eta(I_L, t)}{\partial t} \Big|_{t=0}}{\frac{2\pi}{\lambda_L}\Delta\delta + r_e N_{atm} \lambda_L} \quad (5)$$

Here, we focus on the cutoff energy with $E_q = q\frac{hc}{\lambda_L} = I_p + 3.17U_p$ and introduce a parameter C_d, with which we can control the contribution of Δk_d. Under the critical condition, we have another constraint that the ionization fraction at the peak of the pulse should just reach η_c

$$\eta_c(I_L) = \int_{-\infty}^{0} \frac{\partial \eta(I_L, t)}{\partial t} dt \quad (6)$$

and Eq. 6 can be calculated by the ADK theory (see section S4) (*48*).

Taking argon as an example, as shown in Fig. 3A, Eqs. 5 and 6 are solved by finding the points of intersection of the two curves for different pulse durations, which allows to extract the critical intensities (I_c^{PMC} and I_c^{NCIF}) and the corresponding critical ionization fractions (η_c^{PMC} and η_c^{NCIF}). Obviously, when $C_d = 0$ (solid black line), the solution of Eqs. 5 and 6 is simply reduced to η_c^{PMC}, and the intersections (open triangles) of $\eta_c^{PMC} \approx 2.2\%$ are in excellent agreement with the previous studies (*30*). The predicted I_c^{PMC} and E_{PMC}^{sat} are also in agreement with the experimental results as shown in Fig. 3B. The solutions for η_c^{NCIF} and I_c^{NCIF} under different driving pulse durations are further given by the intersections of the two curves with $C_d \neq 0$ (open squares). Here, an energy upshift of $\Delta E_{qt} \approx 12$ eV is necessary for the agreement of $E_{1\%}^{sat}$, as illustrated in Fig. 3A. With the above method, we can apply the NCIF model to fit the experimental results with only one free parameter, C_d. As shown in Fig. 3x (B and C), remarkably, we find that with $C_d = 0.35$, the model can well reproduce the experimental results under different pulse durations and in different gas atoms (argon and krypton; see section S4).

The NCIF model also explains why there is a limit to the spectral extension under high driving laser intensity, as shown in Fig. 2 (E and F). Under the nonadiabatic conditions, the transient phase matching process can contribute a large amount of positive wave vector mismatch to compensate the negative contribution from the plasma dispersion in Eq. 1, supporting the generation of harmonic orders well above the PMC when the driving laser field is strong and the laser-induced ionization level is high. However, this phase-matching capability has its limit. When $I_L > I_c^{NCIF}$, the gas ionization becomes so high that this compensation is no longer possible. This critical point corresponds to $\eta_c^{NCIF} \approx 13\%$ for $\tau = 9$ fs and $\lambda_L = 1030$ nm, which is several times higher than η_c^{PMC} in argon. This explains the large energy extension of $\Delta E \sim 50$ eV (Fig. 1C). When driven by the longer pulses, η_c^{NCIF} are greatly reduced ($\eta_c^{NCIF} \approx 3.8\%$ for $\tau = 22$ and $\approx 2.4\%$ for $\tau = 170$ fs), as shown in Fig. 3A. The reason is twofold: First, the accumulated gas ionization rises faster for the longer pulses; and second, the time derivative of the gas ionization ($\frac{\partial \eta}{\partial t}$) also reduces when the ionization is high (see section S4), which makes the bending down of the curve for Eq. 6 to occur at lower intensities (Fig. 3A).

The influence of the carrier-envelope phase (CEP) $\Delta\varphi_{CEP}$ is investigated with the NCIF model as shown in Fig. 3 (B and C). We find that the harmonic spectrum varies with a period of π as a function of $\Delta\varphi_{CEP}$, consistent with the previous studies (*29*, *49*, *50*). The model shows that $\Delta\varphi_{CEP}$ has great effects when driven by few-cycle pulses, while its influence becomes negligible when the duration is longer than five optical cycles ($\tau \sim 17$ fs for $\lambda_L = 1030$ nm). Meanwhile, the energy of $E_{1\%}$ is much more strongly affected than E_{PMC}. Our results show that, when $\Delta\varphi_{CEP} = \frac{\pi}{2}$ with the peak field shifted to the pulse leading edge (inset of Fig. 3B), the ionization rate can be reduced, and thereby, the curves of Eqs. 5 and 6 cross at stronger laser intensity, generating higher-energy harmonics. In contrast, when $\Delta\varphi_{CEP}$ approaches $-\frac{\pi}{2}$, the ionization increases because of more optical cycles before the peak field, which yields lower critical intensity in the model. We note that, using the NCIF model, we reveal the phase-matching aspects of the CEP effects, but this model cannot explain the details of the spectral shapes under the modulation of electron trajectories (*49*). It also worth noting that the model results represent the upper limit of the E_{PMC} and $E_{1\%}$ variations, when the laser intensity (I_L) is sufficiently higher than I_c^{NCIF}.

Extension to mid-infrared few-cycle lasers

Here, we extend the NCIF model to longer driving wavelengths and to the gas atoms of neon and helium, which are of great interest for generating high-energy soft x-ray harmonics (*29*, *40*, *41*, *49*, *51*, *52*). In Fig. 3D, we plot the predicted E_{PMC}^{sat} and $E_{1\%}^{sat}$ by the NCIF model for different laser wavelengths (λ_L). The FWHM duration is fixed to be 2.6 cycles and $\Delta\varphi_{CEP} = 0$ in the calculation. To verify our model results, we conducted a series of numerical simulations with different λ_L in neon and helium with $I_L > I_c^{NCIF}$ (solid symbols in Fig. 3D, and see section S3). A typical HHG spectrum obtained from our numerical simulations is plotted in Fig. 3E. The gas pressure is set in the range of 100 to 500 torr for different gas atoms and driving conditions. The three intensity regimes as shown in Fig. 2 (E and F) can also be ubiquitously observed under long-wavelength driving fields (see fig. S5). As shown in Fig. 3D, the NCIF model can yield excellent agreement with the numerical results. We find that the energy extension (ΔE) increases monotonically as a function of λ_L. When driven by a $\lambda_L \sim 2$-μm laser in helium, ΔE could reach ~1 keV, much higher than the corresponding E_{PMC} (~570 eV), leading to an HHG spectrum exceeding 1.5 keV. This is because the contribution of the nonadiabatic dipole-phase term grows quadratically with respect to λ_L (see Eq. 5), which makes the nonadiabatic phase matching play an increasingly important role for longer driving wavelengths. Meanwhile, our model also predicts that, to generate and phase-match these high-energy harmonics, the

Downloaded from https://www.science.org at Universidad de Salamanca on June 29, 2023

driving laser intensity needs to exceed I_c^{NCIF} ≈1300 TW cm^{-2} (see fig. S12), and the corresponding E_{cutoff} is ~1.6 keV in helium when λ_L ~ 2 μm.

DISCUSSION

We note that the C_d parameter is empirically determined in the analytical model. The fact that C_d < 1.0 indicates that the nonadiabatic dipole-phase mismatch (Δk_d) is not fully taken into account (see Eq. 5). First of all, the choice of C_d = 0.35 is related to the fact that we have focused on the phase-matching condition of the 1%-intensity HHG region ($E_{1\%}$), because that is sufficient for routine applications in spectroscopy and imaging. For the 10%-intensity HHG region, the same fitting procedure yields C_d ≈ 0.27 and lower η_c^{NCIF} (see fig. S4). This is expected, because the low-order harmonics can be generated when the driving laser intensity is reduced by the plasma defocusing from the incident intensity of I_L, where both the gas ionization and pulse reshaping become less significant. Second, in the experiments and in the numerical simulations, the HHG may be generated at large beam radii (*29*) or in optical cycles not at the temporal peak, where the driving field intensity is less than I_L. These averaging effects are also empirically considered with this C_d parameter. Although empirical, it is unexpected that a single C_d parameter can be used to characterize the HHG spectral reshaping under the strong nonadiabatic conditions driven by different laser parameters and in different gas media (see Fig. 3, B to D). We believe that the definition of such a parameter, whose interpretation can be justified as explained above, gives an insight on how the nonadiabatic phase matching can be understood. Of course, further detailed analysis should be performed to identify the relationship of C_d with the experimental parameters, but it is beyond of our grasp so far. We further note that, in this work, we have used the geometry where the gas cell is located behind the beam focus. A different C_d parameter may be necessary when a different focusing geometry (*31*) or transverse beam reshaping (*53*) is implemented in the experiments. These methods can influence the dynamics of driving-pulse reshaping, which is the key for the nonadiabatic phase matching of HHG.

In fig. S12, we summarize the results of $E_{1\%}$ observed in the previous experiments driven by few-cycle pulses with different λ_L (*14*, *28*, *29*, *31*, *34*, *41*, *49*–*51*) and compare them with the NCIF model. We find that, for λ_L in the near-infrared region (800 and 1030 nm), the experimental $E_{1\%}$ agrees very well with the NCIF model, while, for the mid-infrared wavelengths (λ_L > 1500 nm), the results are in better agreement with E_{PMC}^{sat} of the model. We believe this can be attributed to two reasons: First, it is still challenging to produce high-intensity few-cycle mid-infrared pulses to exceed I_c^{NCIF} in the experiments. The typical field intensity reported in these works for λ_L > 1500 nm is <500 TW cm^2, which is far below the predicted I_c^{NCIF} (~1300 TW cm^{-2} for helium and ~800 TW cm^{-2} for neon, see fig. S12). Second, our model also shows that the phase-matching pressures for E_{PMC}^{sat} and $E_{1\%}^{sat}$ can be increasingly different for the mid-infrared driving fields. For example, we estimate that the phase-matching pressure of helium at the E_{PMC}^{sat} energy is ~2 atm when λ_L is 800 nm. This pressure grows to tens of atmosphere when the wavelength is increased to 4 μm, in agreement with the previous experiments (*30*). However, in contrast, because of the increasing contribution of the nonadiabatic dipole phase under long driving wavelengths, the phase-matching pressure for $E_{1\%}^{sat}$ decreases from 1 to 0.1 atm when λ_L changes from 800 nm to 4 μm (see fig. S11). This makes it very challenging to simultaneously phase-match both energy regions under a constant gas pressure when the driving wavelength is long. Usually in the experiments, one may focus on the phase matching of the E_{PMC}^{sat} energy to yield the highest harmonic flux, and hence, the harmonic emission beyond PMC can be extinguished by the phase and group velocity mismatches (*54*) under the high gas pressure. In the future, special phase-matching techniques, including predesigned gas cells and gas-filled waveguides (*55*), which can provide inhomogeneous distribution of gas pressure, may be useful to solve this problem. Our results here deliver an optimistic message that it is possible to greatly enhance and extend the HHG brightness and energy to cover the entire soft x-ray range (100 eV to 5 keV) with further development of few-cycle, mid-infrared, and high-intensity lasers. Recent great advances in power-scaling laser technology (*56*), few-cycle pulse-generation

Downloaded from https://www.science.org at Universidad de Salamanca on June 29, 2023

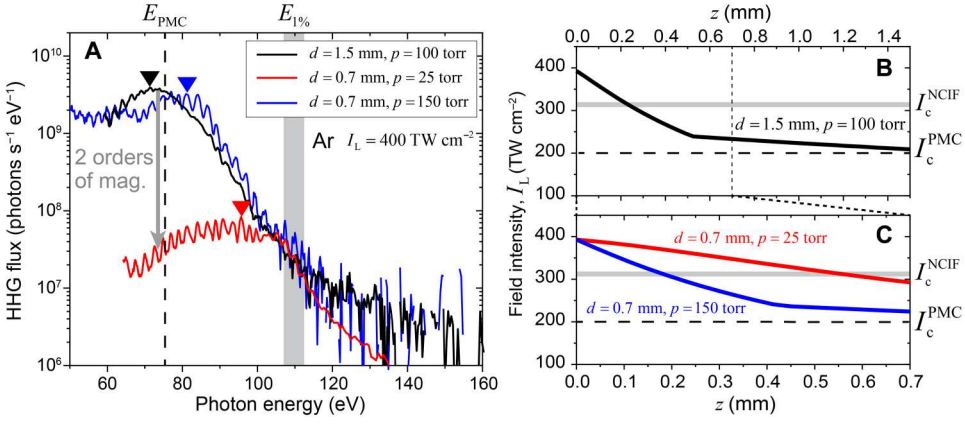

Fig. 4. The nonadiabatic spatial integration effects. (**A**) HHG spectrum in argon obtained under different gas-cell lengths (d) and gas pressure (p). The driving intensity I_L is fixed to be 400 TW cm^{-2} and the pulse duration τ = 9 fs. The energy of E_{PMC} is labeled by solid triangles. (**B**) Peak intensity of the driving field as a function of the propagation distance in the gas cell (z), obtained from the numerical simulation. The critical intensities are labeled for τ = 9 fs, λ_L = 1030 nm in argon, obtained from the NCIF model. (**C**) Same as (B) for different d and p.

techniques (*57*, *58*), and novel wavelength-scaling techniques (*59*, *60*), in combination could achieve this goal in the near future.

The deformation of HHG spectrum resulting from the driving-intensity variation along z (see Fig. 1A) can be clearly demonstrated by the experiments in argon with different medium lengths (d) and gas pressures (p), as shown in Fig. 4A. The incident I_L is ~400 TW cm^{-2}, and the corresponding E_{cutoff} is ~140 eV. We find that, when d is reduced from 1.5 to 0.7 mm at low pressure (p = 25 torr), the propagation in the gas medium is not long enough that the laser intensity remains much higher than I_c^{PMC} throughout the propagation (see Fig. 4C). The high ionization level precludes the phase matching for the harmonics around PMC ~ 75 eV. The harmonic spectrum is reshaped, and we can observe a subsequent upshift of E_{PMC}. We note that, although the pressure-length product is reduced only by a factor of ~8 here, the HHG yield at ~75 eV is reduced by approximately two orders of magnitude (Fig. 4A), highlighting the significant influence of the nonadiabatic effect on the HHG spectral shape. On the other hand, by increasing p to 150 torr at d = 0.7 mm, E_{PMC} and the harmonic yield can be nearly recovered (Fig. 4A). In this case, our simulations show that the increased pressure accelerates the laser-intensity drop along z, making it reduced to around I_c^{PMC} within the 0.7-mm propagation, and this facilitates the phase matching around E_{PMC}. We find that, under all these conditions, the brightness of HHG around $E_{1\%}$ (~120 eV) is almost unaffected. This can be explained by the fact that, in all the three cases, I_L can cross I_c^{NCIF} within the gas medium lengths (see Fig. 4, B and C), which produces these high-energy photons.

In summary, on the basis of the systematic experimental and theoretical investigations of HHG under different driving conditions, we develop a NICF model taking the nonadiabatic effects on the HHG phase matching into account. The model can precisely predict the reshaping and extension of a harmonic spectrum, which is especially important when driven few-cycle mid-infrared lasers. Our results have potential for great impact and widespread use considering the recent great advances in high-energy few-cycle mid-infrared lasers as the driving sources of HHG.

MATERIALS AND METHODS

Experimental setup

The schematic of the experimental setup is shown in the fig. S1. Laser pulses with different pulse durations at a repetition rate of 10 kHz are obtained by compressing the fundamental 170-fs pulses with all-solid-state compressors, which use the soliton management in periodic layered Kerr media (*26*, *61*). In all the experiments, the driving laser beam is focused to a waist (w_0) of 40 to 50 μm through a gas cell with an inner diameter of d = 1.5 or 0.7 mm. The gas cell is typically ~1.5 mm behind the beam focus to ensure the phase matching of short trajectories. The harmonic spectrum is recorded by an XUV spectrometer after filtering out the fundamental driving laser with aluminum or zirconia thin films. The brightness of the harmonic orders is measured with a calibrated photodiode (see section S2).

Numerical simulation

In our numerical simulations, a well-established approach has been used to calculate the electric field of high harmonics emitted from a macroscopic gas target (*39*). Its validity has also been confirmed against experimentally measured HHG spectra from atoms and molecules (*62*, *63*). To fully simulate high harmonics measured in experiment, one needs to consider both single-atom response and macroscopic response from all emitters. First, to calculate the single atom–induced dipole moment caused by the interaction of an atom with the local laser electric field, i.e., single-atom response, the TDSE of the atom under dipole approximation and single-active-electron approximation is solved. We use the quantitative rescattering model to obtain the solution of TDSE, in which the accurate photorecombination cross section obtained in a time-independent manner is applied to replace that in the SFA. An empirically modified ADK model was implemented to take into account the ground-state depletion due to the barrier suppression effect (*43*). Second, to take into account of macroscopic response of gas medium, Maxwell's wave equations (MWEs) for both fundamental driving laser and generated high-harmonic field are solved (*63*). When calculating the propagation of spatiotemporal fundamental driving laser inside the gas medium, the nonlinear effects of diffraction, nonlinear self-focusing, ionization, and medium dispersion are included. Then single atom– induced dipoles at different spatial points are fed into MWEs of the high-harmonic field to account for the propagation effects and phase matching of high harmonics. Meanwhile, the dispersion and absorption of gas medium are included in the MWEs of high-harmonic field. Last, macroscopic HHG spectra can be obtained by integrating high-harmonic yields over the exit plane of gas medium.

Supplementary Materials

This PDF file includes:

Sections S1 to S7
Figs. S1 to S12
References

REFERENCES AND NOTES

1. A. Rundquist, C. G. Durfee, Z. Chang, C. Herne, S. Backus, M. M. Murnane, H. C. Kapteyn, Phase-matched generation of coherent soft x-rays. *Science* **280**, 1412–1415 (1998).
2. Y. Liang, S. Augst, S. L. Chin, Y. Beaudoin, M. Chaker, High harmonic generation in atomic and diatomic molecular gases using intense picosecond laser pulses-a comparison. *J. Phys. B At. Mol. Opt. Phys.* **27**, 5119–5130 (1994).
3. M. Ferray, A. L'Huillier, X. F. Li, L. A. Lompré, G. Mainfray, C. Manus, Multiple-harmonic conversion of 1064 nm radiation in rare gases. *J. Phys. B At. Mol. Opt. Phys.* **21**, L31–L35 (1988).
4. A. Mcpherson, G. Gibson, H. Jara, U. Johann, T. S. Luk, I. A. Mcintyre, K. Boyer, C. K. Rhodes, Studies of multiphoton production of vacuum-ultraviolet radiation in the rare gases. *J. Opt. Soc. Am. B.* **4**, 595–601 (1987).
5. P. M. Paul, E. S. Toma, P. Breger, G. Mullot, F. Augé, P. Balcou, H. G. Muller, P. Agostini, Observation of a train of attosecond pulses from high harmonic generation. *Science* **292**, 1689–1692 (2001).
6. M. Hentschel, R. Kienberger, C. Spielmann, G. A. Reider, N. Milosevic, T. Brabec, P. Corkum, U. Heinzmann, M. Drescher, F. Krausz, Attosecond metrology. *Nature* **414**, 509–513 (2001).
7. Z. Tao, C. Chen, T. Szilvási, M. Keller, M. Mavrikakis, H. Kapteyn, M. Murnane, Direct time-domain observation of attosecond final-state lifetimes in photoemission from solids. *Science* **353**, 62–67 (2016).
8. M. Lewenstein, M. F. Ciappina, E. Pisanty, J. Rivera-Dean, P. Stammer, T. Lamprou, P. Tzallas, Generation of optical Schrödinger cat states in intense laser–matter interactions. *Nat. Phys.* **17**, 1104–1108 (2021).
9. J. L. Krause, K. J. Schafer, K. C. Kulander, High-order harmonic generation from atoms and ions in the high intensity regime. *Phys. Rev. Lett.* **68**, 3535–3538 (1992).
10. M. Lewenstein, P. Balcou, M. Y. Ivanov, A. L'Huillier, P. B. Corkum, Theory of high-harmonic generation by low-frequency laser fields. *Phys. Rev. A* **49**, 2117–2132 (1994).

Downloaded from https://www.science.org at Universidad de Salamanca on June 29, 2023

11. K. J. Schafer, B. Yang, L. F. Dimauro, K. C. Kulander, Above threshold ionization beyond the high harmonic cutoff. *Phys. Rev. Lett.* **70**, 1599–1602 (1993).
12. P. B. Corkum, Plasma perspective on strong-field multiphoton ionization. *Phys. Rev. Lett.* **71**, 1994–1997 (1993).
13. G. Fan, K. Legare, V. Cardin, X. Xie, R. Safaei, E. Kaksis, G. Andriukaitis, A. Pugzlys, B. Schmidt, J. Pierre, M. Hehn, G. Malinowski, B. Vodungbo, E. Jal, J. Luning, N. Jaouen, G. Giovannetti, F. Calegari, Z. Tao, A. Baltuska, F. Légaré, T. Balciunas, Ultrafast magnetic scattering on ferrimagnets enabled by a bright Yb-based soft x-ray source. *Optica* **9**, 399–407 (2022).
14. A. S. Johnson, L. Miseikis, D. A. Wood, D. R. Austin, C. Brahms, S. Jarosch, C. S. Strüber, P. Ye, J. P. Marangos, Measurement of sulfur L2,3 and carbon K edge XANES in a polythiophene film using a high harmonic supercontinuum. *Struct. Dyn.* **3**, 062603 (2016).
15. D. Popmintchev, B. R. Galloway, M. C. Chen, F. Dollar, C. A. Mancuso, A. Hankla, L. Miaja-Avila, G. O'Neil, J. M. Shaw, G. Fan, S. Ališauskas, G. Andriukaitis, T. Balčiunas, O. D. Mücke, A. Pugzlys, A. Baltuška, H. C. Kapteyn, T. Popmintchev, M. M. Murnane, Near- and extended-edge x-ray-absorption fine-structure spectroscopy using ultrafast coherent high-order harmonic supercontinua. *Phys. Rev. Lett.* **120**, 093002 (2018).
16. J. Li, X. Ren, Y. Yin, K. Zhao, A. Chew, Y. Cheng, E. Cunningham, Y. Wang, S. Hu, Y. Wu, M. Chini, Z. Chang, 53-Attosecond X-ray pulses reach the carbon K-edge. *Nat. Commun.* **8**, 186 (2017).
17. T. Gaumnitz, A. Jain, Y. Pertot, M. Huppert, I. Jordan, F. Ardana-Lamas, H. J. Wörner, Streaking of 43-attosecond soft-X-ray pulses generated by a passively CEP-stable mid-infrared driver. *Opt. Express* **25**, 27506 (2017), 27518.
18. A. Rana, J. Zhang, M. Pham, A. Yuan, Y. H. Lo, H. Jiang, S. J. Osher, J. Miao, Potential of attosecond coherent diffractive imaging. *Phys. Rev. Lett.* **125**, 086101 (2020).
19. C. G. Durfee, A. R. Rundquist, S. Backus, C. Herne, M. M. Murnane, H. C. Kapteyn, Phase matching of high-order harmonics in hollow waveguides. *Phys. Rev. Lett.* **83**, 2187–2190 (1999).
20. T. Popmintchev, M. Chen, A. Bahabad, M. Gerrity, P. Sidorenko, O. Cohen, I. P. Christov, M. M. Murnane, H. C. Kapteyn, Phase matching of high harmonic generation in the soft and hard X-ray regions of the spectrum. *Proc. Natl. Acad. Sci. U.S.A.* **106**, 10516–10521 (2009).
21. D. Popmintchev, C. Hernández-García, F. Dollar, C. Mancuso, J. A. Pérez-Hernández, M.-C. Chen, A. Hankla, X. Gao, B. Shim, A. L. Gaeta, M. Tarazkar, D. A. Romanov, R. J. Levis, J. A. Gaffney, M. Foord, S. B. Libby, A. Jaron-Becker, A. Becker, L. Plaja, M. M. Murnane, H. C. Kapteyn, T. Popmintchev, Ultraviolet surprise: Efficient soft x-ray high-harmonic generation in multiply ionized plasmas. *Science* **350**, 1225–1231 (2015).
22. I. P. Christov, M. M. Murnane, H. C. Kapteyn, High-harmonic generation of attosecond pulses in the "single-cycle" regime. *Phys. Rev. Lett.* **78**, 1251–1254 (1997).
23. E. Goulielmakis, M. Schultze, M. Hofstetter, V. S. Yakovlev, J. Gagnon, M. Uiberacker, A. L. Aquila, E. M. Gullikson, D. T. Attwood, R. Kienberger, F Krausz, U. Kleineberg, Single-cycle nonlinear optics. *Science* **320**, 1614–1617 (2008).
24. X. Wang, L. Wang, F. Xiao, D. Zhang, Z. Lü, J. Yuan, Z. Zhao, Generation of 88 as isolated attosecond pulses with double optical gating. *Chin. Phys. Lett.* **37**, 023201 (2020).
25. M. J. Zhan, P. Ye, H. Teng, X. K. He, W. Zhang, S. Y. Zhong, L. F. Wang, C. X. Yun, Z. Y. Wei, Generation and measurement of isolated 160-attosecond XUV laser pulses at 82 eV. *Chin. Phys. Lett.* **30**, 093201 (2013).
26. B. Zhu, Z. Fu, Y. Chen, S. Peng, C. Jin, G. Fan, S. Zhang, S. Wang, C. Tian, Y. Wang, H. Kapteyn, M. Murnane, Z. Tao, Spatially homogeneous few-cycle compression of Yb lasers via all-solid-state free-space soliton management. *Opt. Express* **30**, 2918–2932 (2022).
27. C. Spielmann, N. H. Burnett, S. Sartania, R. Koppitsch, M. Schnürer, C. Kan, M. Lenzner, P. Wobrauschek, F. Krausz, Generation of coherent x-rays in the water window using 5-femtosecond laser pulses. *Science* **278**, 661–664 (1997).
28. R. Klas, W. Eschen, A. Kirsche, J. Rothhardt, J. Limpert, Generation of coherent broadband high photon flux continua in the XUV with a sub-two-cycle fiber laser. *Opt. Express* **28**, 6188–6196 (2020).
29. A. S. Johnson, D. R. Austin, D. A. Wood, C. Brahms, A. Gregory, K. B. Holzner, S. Jarosch, E. W. Larsen, S. Parker, C. S. Strüber, P. Ye, J. W. G. Tisch, J. P. Marangos, High-flux soft x-ray harmonic generation from ionization-shaped few-cycle laser pulses. *Sci. Adv.* **4**, eaar3761 (2018).
30. T. Popmintchev, M. Chen, D. Popmintchev, P. Arpin, S. Brown, S. Ali, G. Andriukaitis, T. Bal, O. D. Mücke, A. Pugzlys, A. Baltu, B. Shim, S. E. Schrauth, A. Gaeta, C. Hernández-garcía, L. Plaja, A. Becker, A. Jaron-becker, M. M. Murnane, H. C. Kapteyn, Bright coherent ultrahigh harmonics in the keV X-ray regime from mid-infrared femtosecond lasers. *Science* **336**, 1287–1291 (2012).
31. J. Schötz, B. Förg, W. Schweinberger, I. Liontos, H. A. Masood, A. M. Kamal, C. Jakubeit, N. G. Kling, T. Paasch-Colberg, S. Biswas, M. Högner, I. Pupeza, M. Alharbi, A. M. Azzeer, M. F. Kling, Phase-matching for generation of isolated attosecond XUV and soft-X-ray pulses with few-cycle drivers. *Phys. Rev. X* **10**, 041011 (2020).
32. C. J. Lai, F. X. Kärtner, The influence of plasma defocusing in high harmonic generation. *Opt. Express* **19**, 22377–22387 (2011).
33. J. A. Pérez-Hernández, L. Roso, A. Zaïr, L. Plaja, Valley in the efficiency of the high-order harmonic yield at ultra-high laser intensities. *Opt. Express* **19**, 19430–19439 (2011).
34. G. Tempea, M. Geissler, M. Schnürer, T. Brabec, Self-phase-matched high harmonic generation. *Phys. Rev. Lett.* **84**, 4329–4332 (2000).
35. M. Geissler, G. Tempea, T. Brabec, Phase-matched high-order harmonic generation in the nonadiabatic limit. *Phys. Rev. A* **62**, 033817 (2000).
36. C. Hernández-García, T. Popmintchev, M. M. Murnane, H. C. Kapteyn, L. Plaja, A. Becker, A. Jaron-Becker, Isolated broadband attosecond pulse generation with near- and mid-infrared driver pulses via time-gated phase matching. *Opt. Express* **25**, 11855–11866 (2017).
37. C. Liu, R. Li, Z. Zeng, Y. Zheng, P. Liu, Z. Xu, Nonadiabatic propagation effect for generating isolated sub-100 as pulses in the high-order harmonic plateau. *Opt. Lett.* **35**, 2618–2620 (2010).
38. E. Constant, D. Garzella, P. Breger, E. Mével, C. Dorrer, C. Le Blanc, F. Salin, P. Agostini, Optimizing high harmonic generation in absorbing gases: Model and experiment. *Phys. Rev. Lett.* **82**, 1668–1671 (1999).
39. M. B. Gaarde, J. L. Tate, K. J. Schafer, Macroscopic aspects of attosecond pulse generation. *J. Phys. B At. Mol. Opt. Phys.* **41**, 132001 (2008).
40. J. Pupeikis, P.-A. Chevreuil, N. Bigler, L. Gallmann, C. R. Phillips, U. Keller, Water window soft x-ray source enabled by a 25 W few-cycle 2.2 μm OPCPA at 100 kHz. *Optica* **7**, 168–171 (2020).
41. M. Gebhardt, T. Heuermann, R. Klas, C. Liu, A. Kirsche, M. Lenski, Z. Wang, C. Gaida, J. E. Antonio-Lopez, A. Schülzgen, R. Amezcua-Correa, J. Rothhardt, J. Limpert, Bright, high-repetition-rate water window soft X-ray source enabled by nonlinear pulse self-compression in an antiresonant hollow-core fibre. *Light Sci. Appl.* **10**, 36 (2021).
42. T. Brabec, F. Krausz, Nonlinear optical pulse propagation in the single-cycle regime. *Phys. Rev. Lett.* **78**, 3282–3285 (1997).
43. X. M. Tong, C. D. Lin, Empirical formula for static field ionization rates of atoms and molecules by lasers in the barrier-suppression regime. *J. Phys. B At. Mol. Opt. Phys.* **38**, 2593–2600 (2005).
44. B. L. Henke, E. M. Gullikson, J. C. Davis, X-ray interactions: Photoabsorption, scattering, transmission, and reflection at E = 50-30,000 eV, Z = 1-92. *At. Data Nucl. Data Tables* **54**, 181–342 (1993).
45. M. Lewenstein, P. Salieres, A. L'Huillier, Phase of the atomic polarization in high-order harmonic generation. *Phys. Rev. A* **52**, 4747–4754 (1995).
46. C. M. Heyl, C. L. Arnold, A. Couairon, A. L'Huillier, Introduction to macroscopic power scaling principles for high-order harmonic generation. *J. Phys. B At. Mol. Opt. Phys.* **50**, 013001 (2017).
47. C. G. Wahlstrom, J. Larsson, A. Persson, T. Starczewski, S. Svanberg, P. Salieres, P. Balcou, A. L'Huillier, High-order harmonic generation in rare gases with an intense short-pulse laser. *Phys. Rev. A* **48**, 4709–4720 (1993).
48. M. V. Ammosov, N. B. Delone, V. P. Krainov, Tunnel ionization of complex atoms and atomic ions in an electromagnetic field. *Sov. Phys.* **64**, 1191–1196 (1986).
49. N. Ishii, K. Kaneshima, K. Kitano, T. Kanai, S. Watanabe, J. Itatani, Carrier-envelope phase-dependent high harmonic generation in the water window using few-cycle infrared pulses. *Nat. Commun.* **5**, 3331 (2014).
50. S. M. Teichmann, F. Silva, S. L. Cousin, M. Hemmer, J. Biegert, 0.5-keV soft X-ray attosecond continua. *Nat. Commun.* **7**, 11493 (2016).
51. P.-A. Chevreuil, F. Brunner, S. Hrisafov, J. Pupeikis, C. R. Phillips, U. Keller, L. Gallmann, Water-window high harmonic generation with 0.8-μm and 2.2-μm OPCPAs at 100 kHz. *Opt. Express* **29**, 32996–33008 (2021).
52. C. Schmidt, Y. Pertot, T. Balciunas, K. Zinchenko, M. Matthews, H. J. Wörner, J.-P. Wolf, High-order harmonic source spanning up to the oxygen K-edge based on filamentation pulse compression. *Opt. Express* **26**, 11834–11842 (2018).
53. H.-W. Sun, P.-C. Huang, Y.-H. Tzeng, J.-T. Huang, C. D. Lin, C. Jin, M.-C. Chen, Extended phase matching of high harmonic generation by plasma-induced defocusing. *Optica* **4**, 976–981 (2017).
54. C. Hernández-García, T. Popmintchev, M. M. Murnane, H. C. Kapteyn, L. Plaja, A. Becker, A. Jaron-Becker, Group velocity matching in high-order harmonic generation driven by mid-infrared lasers. *New J. Phys.* **18**, 073031 (2016).
55. E. A. Gibson, A. Paul, N. Wagner, R. Tobey, D. Gaudiosi, S. Backus, I. P. Christov, A. Aquila, E. M. Gullikson, D. T. Attwood, M. M. Murnane, H. C. Kapteyn, Coherent soft X-ray generation in the water window with quasi-phase matching. *Science* **302**, 95–98 (2003).
56. J.-P. Negel, A. Voss, M. A. Ahmed, D. Bauer, D. Sutter, A. Killi, T. Graf, 11 kW average output power from a thin-disk multipass amplifier for ultrashort laser pulses. *Opt. Lett.* **38**, 5442 (2013).
57. A. Alismail, H. Wang, G. Barbiero, N. Altwaijry, S. A. Hussain, V. Pervak, W. Schweinberger, A. M. Azzeer, F. Krausz, H. Fattahi, Multi-octave, CEP-stable source for high-energy field synthesis. *Sci. Adv.* **6**, eaax3408 (2020).

Downloaded from https://www.science.org at Universidad de Salamanca on June 29, 2023

58. M. Müller, J. Buldt, H. Stark, C. Grebing, J. Limpert, Multipass cell for high-power few-cycle compression. *Opt. Lett.* **46**, 2678–2681 (2021).
59. U. Elu, M. Baudisch, H. Pires, F. Tani, M. H. Frosz, F. Köttig, A. Ermolov, P. St. J. Russell, J. Biegert, High average power and single-cycle pulses from a mid-IR optical parametric chirped pulse amplifier. *Optica* **4**, 1024–1029 (2017).
60. R. Safaei, G. Fan, O. Kwon, K. Légaré, P. Lassonde, B. E. Schmidt, H. Ibrahim, F. Légaré, High-energy multidimensional solitary states in hollow-core fibres. *Nat. Photonics* **14**, 733–739 (2020).
61. S. Zhang, Z. Fu, B. Zhu, G. Fan, Y. Chen, S. Wang, Y. Liu, A. Baltuska, C. Jin, C. Tian, Z. Tao, Solitary beam propagation in periodic layered Kerr media enables high-efficiency pulse compression and mode self-cleaning. *Light Sci. Appl.* **10**, 53 (2021).
62. C. Jin, M.-C. Chen, H.-W. Sun, C. D. Lin, Extension of water-window harmonic cutoff by laser defocusing-assisted phase matching. *Opt. Lett.* **43**, 4433–4436 (2018).
63. C. Jin, A. T. Le, C. D. Lin, Medium propagation effects in high-order harmonic generation of Ar and N_2. *Phys. Rev. A* **83**, 023411 (2011).
64. P. Moreno, L. Plaja, V. Malyshev, L. Roso, Influence of barrier suppression in high-order harmonic generation. *Phys. Rev. A* **51**, 4746–4753 (1995).
65. A. Börzsönyi, Z. Heiner, M. P. Kalashnikov, A. P. Kovács, K. Osvay, Dispersion measurement of inert gases and gas mixtures at 800 nm. *Appl. Optics* **47**, 4856–4863 (2008).

Acknowledgments
Funding: Z.T. gratefully acknowledges support from the National Key R&D Program of China (2021YFA1400202), the National Natural Science Foundation of China (NSFC) (11874121), and the Shanghai Municipal Science and Technology Basic Research Project (19JC1410900). The JILA team graciously acknowledges support from the Department of Energy BES Award No. DE-FG02-99ER14982. H.K. has a coaffiliation as CTO of KMLabs Inc. C.J. acknowledges support from the NSFC under grant nos. 91950102, 12274230, and 11834004 and funding of NJUST under grant no. TSXK2022D005. Y.W. would like to acknowledge partial support by NSFC grant nos. 11827805 and 12150003 and Shanghai Municipal Science and Technology Major Project grant no. 2019SHZDZX01. C.H.-G. acknowledges funding from the European Research Council (ERC) under the European Union's Horizon 2020 research and innovation program (grant agreement no. 851201). G.F. acknowledges support from the Deutsche Forschungsgemeinschaft (DFG, German Research Foundation) via the Cluster of Excellence Advanced Imaging of Matter (AIM).
Author contributions: Z.T., M.M., H.K., and C.J. conceived the project. Z.F., Y.C., S.P., and B.Z. conducted the experiments and analyzed the data. G.F. and Y.W. provided technical support. B.L., C.J., R.M.-H., and C.H.-G. provided theory support. Z.F., Z.T., M.M., H.K., C.J., and C.H.-G. wrote the manuscript with the inputs from the other authors. **Competing interests:** The authors declare that they have no competing interests. **Data and materials availability:** All data needed to evaluate the conclusions in the paper are present in the paper and/or the Supplementary Materials.

Submitted 1 July 2022
Accepted 17 November 2022
Published 23 December 2022
10.1126/sciadv.add7482

Downloaded from https://www.science.org at Universidad de Salamanca on June 29, 2023

ScienceAdvances

Extension of the bright high-harmonic photon energy range via nonadiabatic critical phase matching

Zongyuan Fu, Yudong Chen, Sainan Peng, Bingbing Zhu, Baochang Li, Rodrigo Martn-Hernndez, Guangyu Fan, Yihua Wang, Carlos Hernndez-Garca, Cheng Jin, Margaret Murnane, Henry Kapteyn, and Zhensheng Tao

Sci. Adv., **8** (51), eadd7482.
DOI: 10.1126/sciadv.add7482

View the article online
https://www.science.org/doi/10.1126/sciadv.add7482
Permissions
https://www.science.org/help/reprints-and-permissions

Downloaded from https://www.science.org at Universidad de Salamanca on June 29, 2023

Use of this article is subject to the Terms of service

Science Advances (ISSN) is published by the American Association for the Advancement of Science. 1200 New York Avenue NW, Washington, DC 20005. The title *Science Advances* is a registered trademark of AAAS.
Copyright © 2022 The Authors, some rights reserved; exclusive licensee American Association for the Advancement of Science. No claim to original U.S. Government Works. Distributed under a Creative Commons Attribution NonCommercial License 4.0 (CC BY-NC).